PROCEEDINGS A

rspa.royalsocietypublishing.org

Research

Article submitted to journal

Subject Areas:
mechanical engineering, materials science

Keywords:
cellular automata, finite elements, cleavage, polycrystals, grain boundary, three-dimensional, Fortran, coarrays

Author for correspondence:
A. Shterenlikht
e-mail: mexas@bris.ac.uk

Three-dimensional cellular automata modelling of cleavage propagation across crystal boundaries in polycrystalline microstructures

A. Shterenlikht[1], L. Margetts[2]

[1]Mech Eng Dept, The University of Bristol, Bristol BS8 1TR, UK
[2]Directorate of IT Services, The University of Manchester, UK and Oxford e-Research Centre, The University of Oxford, UK

A three-dimensional cellular automata with rectilinear layout is used in this work to create and cleave polycrystalline microstructures. Each crystal is defined by a unique randomly generated orientation tensor. Separate states for grains, grain boundaries, crack flanks and crack fronts are created. Algorithms for progressive cleavage propagation though crystals and across grain boundaries are detailed. The mesh independent cleavage criterion includes the critical cleavage stress and the length scale. Resolution of an arbitrary crystallographic plane within a 26-cell Moore neighbourhood is considered. The model is implemented in Fortran 2008 coarrays. The model gives realistic predictions of grain size and mis-orientation distributions, grain boundary topology and crack geometry. Finally we show how the proposed cellular automata model can be linked to a finite element model to produce a multiscale fracture framework.

THE ROYAL SOCIETY
PUBLISHING

© The Author(s) Published by the Royal Society. All rights reserved.

1. Introduction

Cellular automata (CA) modelling of physical systems is a well established field [1–3]. CA is a discrete time - discrete space framework. The model space is partitioned into identical *cells* with a finite number of states. A state of a cell at the next time increment is determined by the state of this cell and the states of some *neighbourhood* at the previous time increment. Fixed or self-similar model boundaries can be used. This simple framework gives rise to a surprisingly rich range of behaviours, some of which are suitable for simulating physical processes such as lattice gas diffusion, phase transitions, wave propagation, multi-phase fluids [2]. In solid mechanics it is popular to superimpose continuum fields, such as temperature, stress or strain, over the CA space. A combination of CA and finite elements, sometimes referred to as CAFE or CA-FE, has been used successfully for predicting ductile to brittle transitional fracture [4], oxide cracking in hot rolling [5], grain instability [6], solidification [7,8], friction stir welding [9], recrystallisation [10–13] and dynamic strain induced transformation [14].

The vast majority of CA models explored over the years are two-dimensional. However, there are physical processes which cannot be accurately represented by 2D models. Polycrystalline fracture is one example. Specifically, transgranular cleavage propagation across grain boundaries cannot be modelled adequately by a 2D model, because grain boundary accommodation failure, due to mis-orientation of preferred cleavage planes in the neighbouring grains, cannot be taken into account [15–17].

It is important to highlight the major difference between the cellular automata approach and Voronoi tessellation [18,19]. The crystals produced by the Voronoi method have easy geometrical description: faces, edges, vertices. In contrast a CA produced crystal is just a collection of connected cells. A CA grain has neither faces, nor edges or vertices. This might appear to be a disadvantage. However, one must remember that Voronoi polyhedra is an idealisation of crystal shapes in real polyscrystalline materials. Indeed, one might argue that 'blobs' of irregular shape, produced by the CA approach, are closer to nature, as seen through the microscope, than nicely defined Voronoi polyhedra. However, the major advantage of the CA approach over the Voronoi tessellation is in the ability of the CA framework to model grain competition, recrystallisation, grain boundary migration and other phenomena resulting in the evolution of the microstructure. This is easily achieved in the CA model, precisely because the crystals are not defined by the geometric means. Evolution of microstructure will require a lot more work if is to be implemented via the Voronoi tessellation approach. However, Voronoi tessellation can be useful for setting the initial cellular morphology [10].

This paper is concerned with the design of a 3D CA model, feature rich and flexible enough to represent a wide range of polycrystalline microstructures and transgranular cleavage propagation in those.

The following notation is used in this work. Tensors of rank 2 are shown in bold: $\mathbf{R}$. Vectors and scalars are in the upright math type: x. Cell states are sans serif: c.

2. The cellular automata model

A 3D CA space with cubic cells and 26-cell Moore neighbourhood is created. The CA model is a rectilinear brick with d_1, d_2 and d_3 cells along dimensions 1,2 and 3 respectively. The total number of cells in the model is $D = d_1 \times d_2 \times d_3$.

First a polycrystalline grain microstructure is created by a simple solidification process in the following way. All cells are initially considered to be of liquid state, $\mathsf{c}_L = 0$. N randomly chosen cells represent grain nuclei. These are assigned states $\mathsf{c}_G \in [1 \dots N]$. Each grain (single crystal) is assigned a randomly chosen orientation tensor, $\mathbf{R}^c$. Each iteration of the solidification process a liquid cell can acquire the state of one of the 26 randomly chosen neighbours. This is shown schematically in Fig. 1. This process is continuing until there are no liquid cells left in the model. Both fixed and self-similar boundary conditions can be used [6].

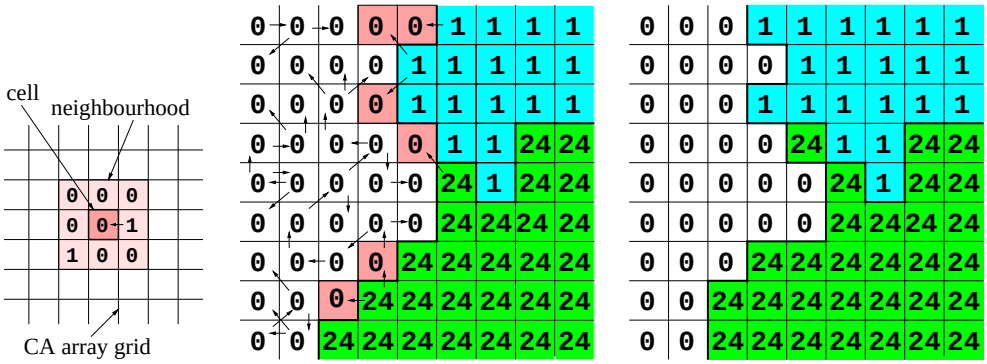

Figure 1. (a) A 2D slice of the 3D 26-cell Moore neighbourhood, showing a central liquid cell, c $= 0$, acquiring the state of one randomly chosen neighbour, indicated by an arrow, grain number 1, c $= 1$, in this example; (b) and (c) A 2D illustration of a single iteration of 3D solidification. Six liquid cells changed state to solid in this increment; three cells attached to grain 1, and the other three attached to grain 24. The arrows show the copying of cells states.

The model described above will produce equiaxed microstructure. By changing the initial distribution of grain nuclei, other popular distributions can be easily achieved, e.g. bimodal or columnar [6]. Our prior work suggested that, in order to achieve results independent of grain resolution, the CA model must be created with a sufficient resolution, $N/D < 10^{-5}$ i.e. more than 10^5 cells must be used, on average, to represent each grain [6].

A CA method itself has no concept of length or time scales. These scales are assigned to CA by the user, based on the exact physical process of interest. In relation to this work, this means that a polycrystal structure produced by the above algorithm can represent micro- or nano-crystal structures. One major difference between nano- and micro-crystalline materials is that in nano-materials the volume occupied by grain boundary regions becomes comparable to that occupied by grain interiors. The fraction of grain boundary volume could be as high as 50% or even more [20,21]. This result emerges naturally from this CA model. If one considers all cells having neighbours belonging to other grains, as *grain boundary cells*, then their number (volume) will increase dramatically with decreasing mean grain size.

3. The quasi-cleavage algorithm

We use tensor, index-free, notation. All sub- and super-scripts are not to be confused with lower and upper indices of index notation.

Orientation of each crystal with respect to the spatial (cellular) coordinate system (CS) is given by the rotation tensor, $\mathbf{R}^c$, with the usual meaning: a vector in the crystal CS, $\mathbf{x}^c$, is transformed into a vector in the spatial CS, $\mathbf{x}^s$, as $\mathbf{x}^s = \mathbf{R}^c \cdot \mathbf{x}^c$.

The stress tensor in the spatial CS, $\mathbf{t}^s$, is transformed into the stress tensor in the crystal CS as $\mathbf{t}^c = \mathbf{R}^s \cdot \mathbf{t}^s \cdot \mathbf{R}^{-s}$, where $\mathbf{R}^s \equiv \mathbf{R}^{-c} \equiv (\mathbf{R}^c)^{-1} \equiv (\mathbf{R}^c)^T$.

It is assumed that cleavage is controlled by the normal stress on a crystallographic plane, t^n. For a plane {hkl}, with normal $\mathbf{n}_{hkl}$, the normal stress is $t_{hkl} = \mathbf{n}_{hkl} \cdot \mathbf{t}^c \cdot \mathbf{n}_{hkl}$.

Each crystallographic plane is assumed to have a particular surface energy, γ_{hkl}. We postulate that the work of cleavage is equal to the surface energy. It is further assumed that the work of cleavage is t_{hkl} times the distance necessary to break the atomic bonds. Following Gilman [22], this distance is taken equal to a_0, the relaxation distance, which is the atom diameter in the cleavage plane. The cleavage condition is $t_{hkl} a_0 = \gamma_{hkl}$, from which the stress required to cleave the {hkl} plane can be calculated:

$$t_{hkl} = \gamma_{hkl}/a_0 \tag{3.1}$$

Example values for iron, from [22], are $\gamma_{100} = 1440$, $\gamma_{110} = 1710$ and $\gamma_{111} = 5340$ erg/cm^2 (1erg/cm^2 = 10^{-3}J/m^2) and $a_0 = 1.37 \times 10^{-10}$m. This gives: $t_{100} = 1.05 \times 10^4$MPa, $t_{110} = 1.25 \times 10^4$MPa, $t_{111} = 4.90 \times 10^4$MPa.

In a CA model these values must be scaled down, because the CA model is not applicable at the atomic scale but only at some intermediate, meso-scale, and because material imperfections and micro-plasticity elevate the stresses locally around the crack fronts [23]. Micro-plasticity has not yet been implemented in this model. Hence, in strict terms, the results are valid for some simplified polycrystalline material. This is the reason we use the term *quasi-cleavage* instead of simply cleavage.

When the cleavage condition of Eqn. (3.1) is satisfied, the model crack advances for a *characteristic length*, which must be taken smaller than the corresponding characteristic length in the model, e.g. the mean grain size. Together the cleavage criterion and the characteristic cleavage length form a cleavage model independent of the CA resolution.

More complex cleavage criteria have been proposed in the literature. These are based on detailed molecular dynamics and quantum mechanics analysis of inter-atomic bond potential, and formulation of cohesive zone type bond breaking models [24–26].

In bcc crystals there are 24 symmetric rotation tensors, $\mathbf{R}_{sym}^{1\ldots24}$, including the identity tensor. If $\mathbf{n}_{hkl}$ is a unit normal vector to some {hkl} plane, then $\mathbf{n}_{hkl}^{1\ldots24} = \mathbf{R}_{sym}^{1\ldots24} \cdot \mathbf{n}_{hkl}$ are 24 normal vectors describing planes of the same class. The weakest plane is that which maximises t_{hkl}:

$$t_{hkl}^{\max} = \max_{hkl}(t_{hkl}) = \max_{i=1\ldots24}(\mathbf{n}_{hkl}^{i} \cdot \mathbf{t}^{c} \cdot \mathbf{n}_{hkl}^{i}) \tag{3.2}$$

where the only planes under consideration are {100}, {110} and {111}, although the surface energy of {111} planes is so high that it is practically impossible to cleave those. The normals to the planes of the maximum normal stress are $\mathbf{n}_{100}^{\max}$, $\mathbf{n}_{110}^{\max}$ and $\mathbf{n}_{111}^{\max}$. From Eqn. (3.1) cleavage will occur when $t_{hkl}^{\max} \geq \gamma_{hkl}/a_0$, or when $p_{hkl}^{\max} = t_{hkl}^{\max}/(\gamma_{hkl}/a_0) \geq 1$.

The first step is to find all $p_{hkl}^{\max}$ and the orientations of the corresponding planes, Alg. 1. The second step is choosing the weakest plane and setting the cleavage cell state accordingly, Alg. 2. The outputs are the unit vector, $\mathbf{n}^s$, normal to the active cleavage plane, in the spatial CS, and the cleavage cell state, s. Vector $\mathbf{n}^c$ is first calculated in the crystal CS and then rotated to the spatial CS, $\mathbf{n}^s$. Cell states $\mathsf{c}_{100}, \mathsf{c}_{110}, \mathsf{c}_{111}$ represent cleavage crack *edges* on {100}, {110}, {111} planes. The flag is *true* if cleavage condition is met, and *false* otherwise.

Algorithm 1: Cleavage algorithm, calculating maximum normal stresses and their planes

input : $\mathbf{t}^s$, $\mathbf{R}^c$, γ_{100} , γ_{110} , γ_{111} , a_0
output: p_{100} , p_{110} , p_{111} , $p^{\max}$, $\mathbf{n}_{100}^{\max}$, $\mathbf{n}_{110}^{\max}$, $\mathbf{n}_{111}^{\max}$
$\mathbf{t}^c = \mathbf{R}^{-c} \cdot \mathbf{t}^s \cdot \mathbf{R}^c$
$t_{100}^{\max} = \max_{i=1\ldots24}(\mathbf{n}_{100}^{i} \cdot \mathbf{t}^c \cdot \mathbf{n}_{100}^{i}) \rightarrow \mathbf{n}_{100}^{\max}$
$t_{110}^{\max} = \max_{i=1\ldots24}(\mathbf{n}_{110}^{i} \cdot \mathbf{t}^c \cdot \mathbf{n}_{110}^{i}) \rightarrow \mathbf{n}_{110}^{\max}$
$t_{111}^{\max} = \max_{i=1\ldots24}(\mathbf{n}_{111}^{i} \cdot \mathbf{t}^c \cdot \mathbf{n}_{111}^{i}) \rightarrow \mathbf{n}_{111}^{\max}$
$p_{100} = t_{100}^{\max}/(\gamma_{100}/a_0)$; $p_{110} = t_{110}^{\max}/(\gamma_{110}/a_0)$; $p_{111} = t_{111}^{\max}/(\gamma_{111}/a_0)$
$p^{\max} = \max(p_{100}, p_{110}, p_{111})$

4. Cleavage representation in the cellular model

In the fracture cellular array, cells are initially *intact*. A number of crack nuclei, i.e. cells with cleavage crack edge states, c_{100} or c_{110}, are positioned within the model. For example, the crack nuclei can be scattered at random, representing pre-existing micro- or nano-cracks in the material. In this manner, growth and/or interaction of a single or multiple cracks can be modelled.

Algorithm 2: Cleavage algorithm, calculating the cleavage plane

input : p_{100} , p_{110} , p_{111} , $p^{\max}$, $\mathbf{n}_{100}^{\max}$, $\mathbf{n}_{110}^{\max}$, $\mathbf{n}_{111}^{\max}$
output: $\mathbf{n}^s$, s , flag
$\mathbf{n}^s = \mathbf{0}$; $\mathsf{s} = 0$; flag = *false*
if $p^{\max} \geq 1$ **then**
  cleavage on {110} plane → flag = *true* ; $\mathbf{n}^c = \mathbf{n}_{100}^{\max}$; $\mathsf{s} = \mathsf{c}_{100}$
  if $p_{110} > p_{100}$ **then**
    cleavage on {110} plane → $\mathbf{n}^c = \mathbf{n}_{110}^{\max}$; $\mathsf{s} = \mathsf{c}_{110}$
  if $p_{111} > p_{100}$ **and** $p_{111} > p_{110}$ **then**
    cleavage on {111} plane → $\mathbf{n}^c = \mathbf{n}_{111}^{\max}$; $\mathsf{s} = \mathsf{c}_{111}$
  $\mathbf{n}^s = \mathbf{R}^c \cdot \mathbf{n}^c$

Next we scan over all intact cells. If an intact cell has a cleaved neighbour, such that the vector connecting the cleaved and the intact cells, $\mathbf{e}$, is on or near the cleavage plane, then the state of the central cell is changed to the given cleavage state. Note that it is possible that the given cleavage state and the neighbour cleavage state will differ. The key decision in this approach is choosing a suitable threshold, t, for deciding when $\mathbf{e}$ belongs to the cleavage plane, defined by $\mathbf{n}^s$. This problem is analysed in Appendix A. Assuming that such threshold can be chosen, the algorithm is summarised in Alg. 3.

Algorithm 3: Cleavage algorithm, propagating cleavage crack through the cellular model.

input : $\mathbf{n}^s$, s , t
output: cell state change

for *all cells* **do**
  pick cell i
  for *all 26 neighbours of* i **do**
    pick neighbour j
    if *cell* j *cleaved* **then**
      $\mathbf{e}$ is a unit vector connecting cells i and j
      if $\mathbf{e} \cdot \mathbf{n}^s < t$ **then**
        cell i state is changed to s
        exit

The cleavage criterion can be easily changed from a fully deterministic to a probabilistic, e.g. if $\mathbf{e} \cdot \mathbf{n}^s < t$ then there is a *probability* that the state of cell i is changing to c. This probability will be inversely related to $\mathbf{e} \cdot \mathbf{n}^s$.

Alg. 3 changes states only of the neighbouring cells. Thus the speed of cleavage propagation in this algorithm is 1 cell/increment. With the use of the characteristic length scale, any crack propagation speed is achievable.

Algs. 1, 2 and 3 are combined to simulate cleavage propagation across the whole cellular grain array G. The algorithm grows cracks in a similar way to grain growth algorithm: any intact cell of the fracture array F is allowed to join a cleavage crack if the following 3 conditions are met: (1) it has a neighbouring crack front cell, (2) it lies on the cleavage plane and (3) the resolved stress is high enough. If $\mathbf{t}^c$ is changing very slowly, compared to the cleavage propagation speed, Algs. 1 and 2 need to be run only when the grain boundary is crossed, i.e. when the current cell, g_i, in the grain array, G, differs from the state of the neighbour, g_{old}. The resulting algorithm is shown

in Alg. 4. However, Alg. 4 does not take into account the full complexity of cleavage propagation across a grain boundary in 3D, see e.g. [15,27,28].

Algorithm 4: Complete cleavage algorithm, top level view.

input : grain cellular array G , fracture cellular array F , $\mathbf{R}^c$ array , $\mathbf{t}^s$
output: possible cell state change to cleaved
$g_{old} = 0$
for *all cells in* F **do**
  pick cell i ; read its grain number g_i ; read its fracture state f_i
  if $f_i = intact$ **then**
    if $g_i \neq g_{old}$ **then**
      run Algs. 1, 2 $\rightarrow \mathbf{n}^s$, s , flag
      $g_{old} = g_i$
    if *flag* = *true* **then**
      run Alg. 3 $\rightarrow$ change f_i to s

5. Crossing a grain boundary

The influence range in a CA model is one cell size. In this respect CA is closer to a molecular dynamics approach, albeit on larger spatial and time scales, where the energy potentials are invariably of a very close range, than to a weak formulation of continuum mechanics, where some form of global equilibrium is usually maintained. Creating and maintaining global entities, such as geometrical planes, edges or vertices, is very computationally expensive in CA formulation. In CA a grain boundary is simply a cluster of cells of identical state g_i, each of which has a neighbour of a different type, g_j. Although it would be possible, in principle, to fit a plane over this cluster, e.g. via a linear minimisation, this is not done in this work due to high computational costs. A grain boundary edge is a cluster of cells of identical state, each of which has neighbours of at least *two* different states.

Analysis of grain boundary fracture typically involves quantities such as crystallographic types of grain boundaries and grain boundary plane orientation. These quantities are not available in this CA formulation. Hence, simulating cleavage propagation across a grain boundary involves some extra considerations, compared to approaches where grains are modelled as polyhedra, see e.g. [15]. In such geometrical (global) model the process is simple: as soon as a cleavage crack reaches a grain boundary at some spatial point, a cleavage plane in the following, adjacent, grain is fully determined, thus allowing for the analysis of the fracture of the boundary fragment defined by the grain boundary plane and by the two cleavage planes in both grains.

In contrast, in a cellular (local) model, there is no global cleavage plane defined in a grain. Hence each crack front cell at the grain boundary has a a chance of starting a new cleavage crack in the adjacent grain. If left unchecked, this process quickly leads to a proliferation of cleavage cracks on multiple parallel crystallographic planes in the next grain. This situation is shown schematically in Fig. 2. Such a model is, of course, not physical. It must not be confused with river patterns which are sometimes seen in cleavage fracture surfaces (see e.g. [29] and references thereof).

Note that the geometrical model is not physical either. It simply looks at the final result of the cleavage propagation and tries to reproduce it. It is doubtful that the physical reality of cleavage propagation across the grain boundary is close to the global geometrical view.

To prevent the nonphysical cleavage crack proliferation scenario illustrated in Fig. 2, only the first cleavage crack cell that touches the grain boundary is allowed to start a new cleavage crack

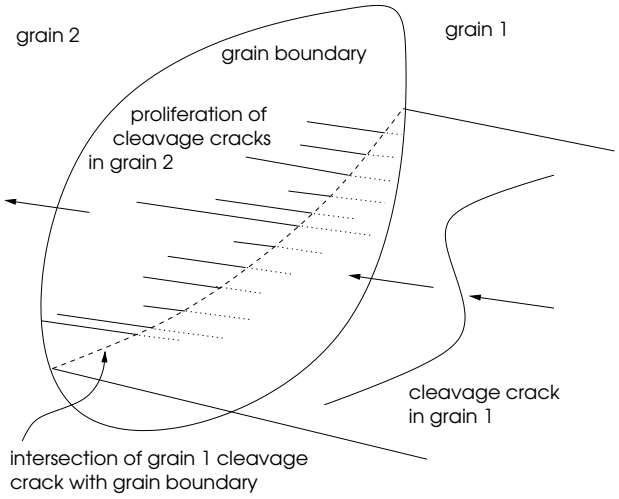

Figure 2. Schematic of cleavage crack proliferation at grain boundary crossing due to using only the local neighbourhood CA analysis. The arrows show the predominant cleavage propagation direction, from right (grain 1) to left (into grain 2). The dashed line represents the intersection of the cleavage crack in grain 1 with the grain boundary. Note that a single cleavage crack in grain 1 can initiate cleavage cracks in grain 2 at any point where it crosses the grain boundary.

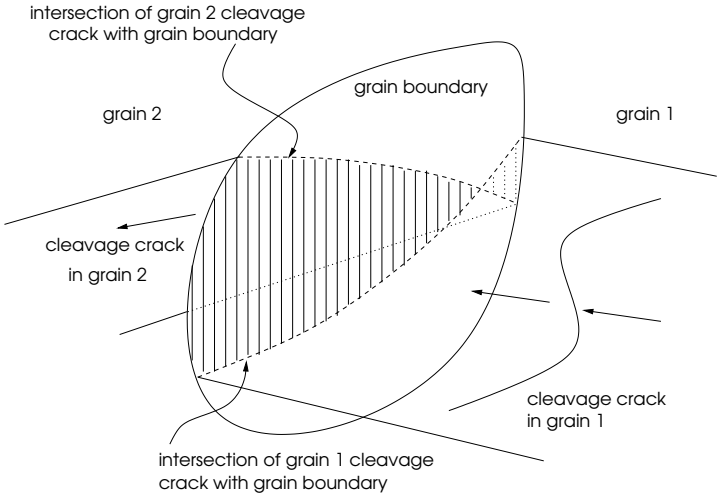

Figure 3. Schematic of the accommodation failure of the grain boundary to allow a complete separation of the model due to a running cleavage crack. The region of the boundary that has to fail to allow for a complete separation is shown hatched. This is a conventional interpretation of grain boundary accommodations failure, see e.g. [16].

in the adjacent grain. The grain boundary is marked as failed immediately, and after that no other cleavage crack is permitted to cross this grain boundary. To this end the grain boundary connectivity array is created at the beginning of the cleavage simulation. The array contains an entry for each grain boundary, which is *inact* initially, and is updated to *failed* when crossed by a cleavage crack. A failed grain boundary cannot be crossed by another cleavage crack.

Another problem is that of simulating the accommodation failure of the grain boundary, to allow for a complete separation of the parts of the model. The region of accommodation failure is shown hatched in Fig. 3. Again, the local nature of the CA approach makes this hard, because the

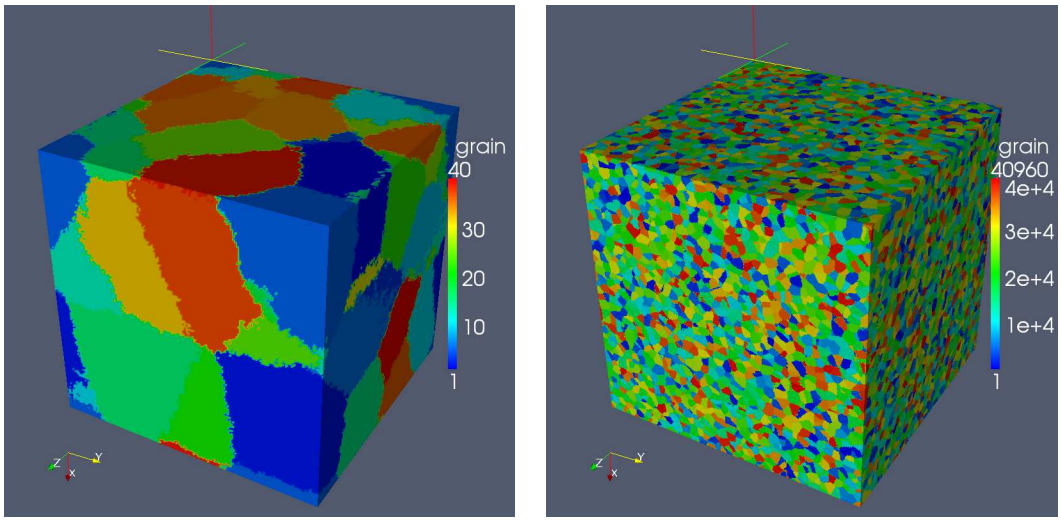

(a) (b)

Figure 4. Two examples of simulated equiaxed polycrystalline microstructures, showing a cubic volume populated with (a) 40 grains, and (b) 40,960 grains. The scale is arbitrary. Gray scale (colour version online) denotes a unique grain number that is linked with a randomly assigned rotation tensor, $\mathbf{R}^c$. Hence if the spatial volumes in (a) and (b) are considered identical, then the mean grain size in (b) is smaller than in (a). Alternatively, if the mean grain size is considered identical in (a) and (b), then example (b) represents a much bigger spatial volume of material than (a).

knowledge of global geometrical quantities is required, specifically the relative spatial orientation of the regions of the grain boundary with respect to the cracks on both sides of the boundary. In the absence of this information, when a grain boundary cell is analysed, the immediate neighbourhood information is insufficient to decide whether the cell should fail or not.

6. Results

The model was implemented in modern Fortran 2008 [30]. The code is available under 2-clause BSD licence from http://sourceforge.net/projects/cgpack/. The code uses coarrays for portability and performance. It is designed to be highly scalable so that it can be used on high performance computers. The code has shown good scalling up to 32,000 processors on HECToR, the UK national supercomputer [31].

Fig. 4 shows 2 examples of simulated equiaxed microstructures. In both cases a cubic volume was modelled. In the first case it was populated with 40 grains, and in the second example 40,960 grains were grown.

Fig. 5 shows two predicted grain size histograms, with 5,120 grains, Fig. 5(a) and with 40,960 grains, Fig. 5(b). The value of this data is that it allows for a direct comparison with the experimental measurement. Another expected, but still very important, result is that the maximum grain size in the model is increasing with the model size. For the model with 5,120 grains the biggest grain is about 3.5 times bigger than the mean, Fig. 5(a), while for the model with 40,960 grains, the biggest grain is 4 times the mean size, Fig. 5(b). This observation is important because cleavage is often thought of as the weakest link model, and the largest grains will have the lowest toughness [32]. Hence the bigger the model, the higher the chances of representing an extremely low fracture energy event.

Fig. 6 shows two important predictions obtained with a 640 grain model of an equiaxed microstructure with periodic (self-similar) boundary conditions. Fig. 6(a) shows the predicted grain boundary mis-orientation distribution. The model prediction closely matches the theoretical results of [33]. The maximum calculated value is 62.5°, whereas the theoretical maximum is 62.8°.

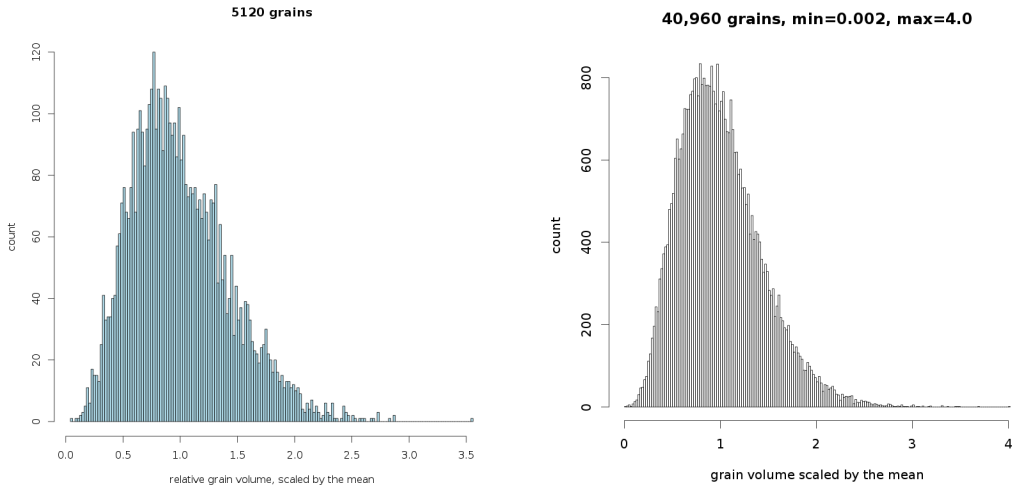

(a) (b)

Figure 5. Grain size histograms from simulated equiaxed microstructures, showing (a) data from the model with 5,120 grains, and (b) data from the model with 40,960 grains, shown in Fig. 4(b). Note the increase in the relative size of the biggest grain with increasing the number of grains in the model.

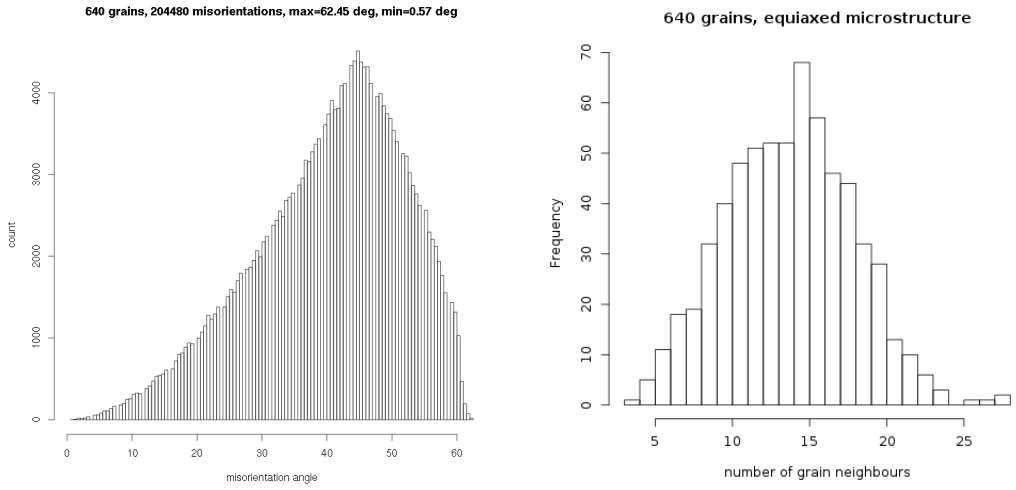

(a) (b)

Figure 6. Useful predictions from a 640 grain equiaxed microstructure model, showing (a) the histogram of predicted grain boundary mis-orientations in an equiaxed microstructure. The shape, the peak (45°) and the maximum angle (62.45°) match the theoretical predictions given e.g. in [33]; and (b) the histogram of the number of neighbouring grains, which roughly follows the normal distribution, with the mean around 15 neighbours. Note that this prediction is not easy to validate experimentally because most, if not all experimental measurements of microstructures are done on 2D slices, and 3D information can be extrapolated only using some additional assumptions.

Fig. 6(b) shows the predicted distribution of the number of neighbouring grains. The mean value is around 15 neighbours, whereas in 3D geometric models, with the popular 14-hedra grain shape (the Kelvin polyhedron), each grain has 14 neighbours sharing a face [15,34]. This similarity is all

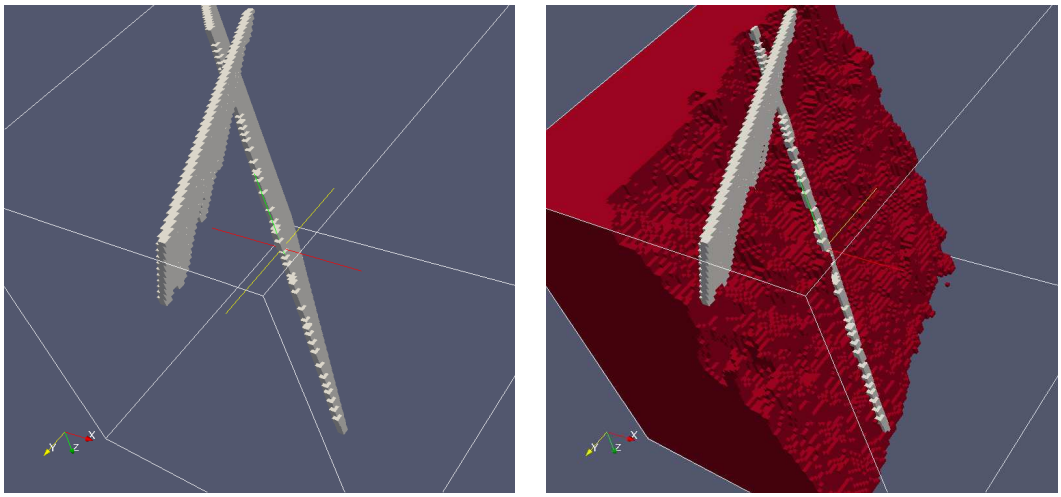

(a) (b)

Figure 7. A model with 2 randomly oriented grains and a single cleavage micro-crack at a randomly chosen location in grain 1, showing (a) Two {100} cleavage cracks in both grains, with grain cells removed for clarity, and (b) the same superimposed with grain 1. Note an irregular grain boundary and irregular intersections of both cracks with the grain boundary.

the more striking given that a grain in a cellular model has no defined faces, edges or vertices. This comparison adds validity to the 3D cellular automata grain modelling results.

Fig. 7 shows an example of a model with 2 grains, with fixed boundary conditions, in which a single cleavage micro-crack, i.e. a cleavage nuclei cell, was assigned a random location in grain 1. The results show the state of the model after 70 cleavage iterations. Both cracks are on {100} planes. Discretisation of a randomly oriented plane within a 26 cell neighbourhood is very coarse, see Appendix A. This means that two planes of a different orientation, passing through the same cell, might be discretised identically, unless their orientations are substantially different. In some cases the mis-orientation angle must be 45° for the planes to be discretised differently in a cellular model. Appendix A gives more details.

The grain boundary, and the intersections of both cracks with the grain boundary are irregular, i.e. hard to describe by global geometrical parameters, see Fig. 7. We note that there is a school of thought that insists that fractal geometry, rather than differential geometry, is the only meaningful approach when dealing with polycrystalline fracture surfaces [35–39]. Also note that the grain boundary area between the two intersections with the cleavage cracks in Fig. 7(b) would ultimately fail by some other mechanism, possibly ductile shear [15,16,22,27–29]. This modelling result is consistent with the theoretical framework, see Fig. 3 and [15,16].

Fig. 8 shows an example of non-physical 1D cracks. This is an artifact of allowing only 2 neighbouring cells to be associated with the cleavage plane passing through the central cell in Alg. 3. As shown in Appendix A, if $t = 0.1733$, then for any $\mathbf{n}^s$ there will always be at least 2 neighbouring cells on the cleavage plane. As the orientation of these 2 cells with respect to the the central cell are always the same, as long as $\mathbf{n}^s$ is constant, the only possible resulting crack shape is 1D straight lines. An intuitive solution to this problem is to increase t "a little bit", to make sure there are always at least 4 neighbouring cells on the cleavage plane. However, in this case there are such $\mathbf{n}^s$ directions, for which the neighbouring cells considered to lie on the cleavage plane are not on the same geometrical plane. Alg. 3 then results in 3D cracks, which are equally non-physical, see Fig. 9.

Fig. 10 shows the the grain boundary accommodation fracture for the two {110} cleavage cracks. As described in Sec. 4, at present, we have no good physically sound local criteria to

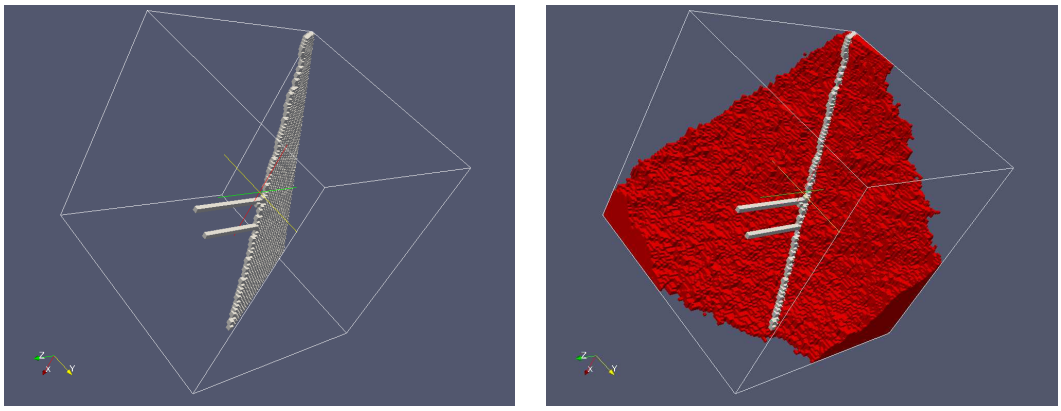

(a) (b)

Figure 8. An example of 1D cracks produced, when only 2 neighbouring cells are recognised as lying on the cleavage plane. This is a rare but possible modelling artifact when the threshold, $t = 0.1733$. See section 4 and Appendix A for more details. This fixed boundary model included 2 grains. (a) The {100} crack is planar in grain 1, but the cracks in grain 2 are discretised as 1D linear cracks. The grains are not shown for clarity. (b) Grain 1 and the grain boundary are superimposed on the cracks. Note the irregularity of the grain boundary.

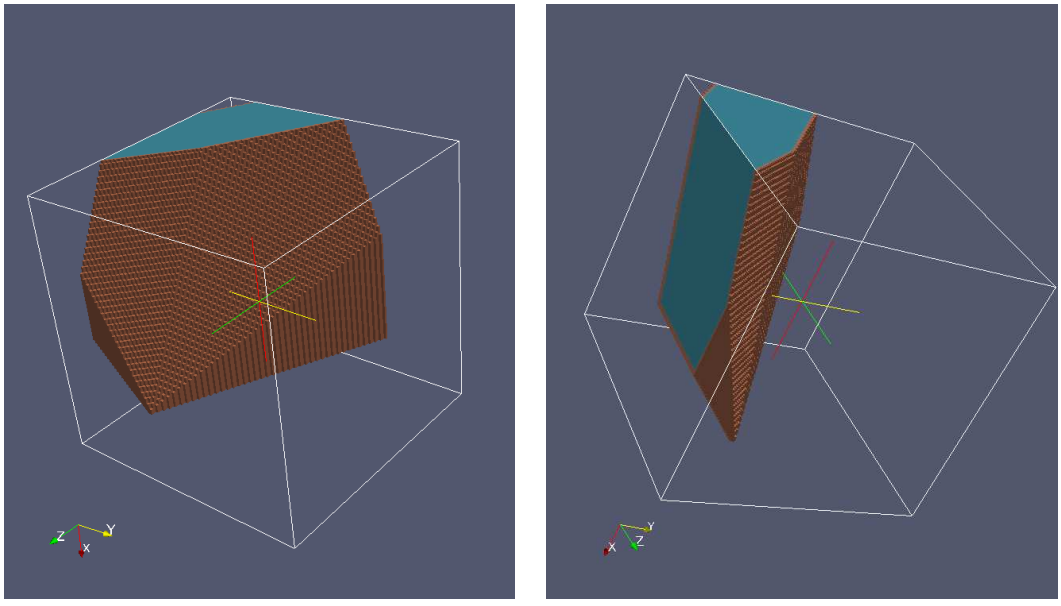

(a) (b)

Figure 9. Two views of the same nonphysical 3D crack. This is a rare but possible artifact of the 3D cellular model if the threshold, $t > 0.1733$.

decide which parts of the grain boundary should fail to achieve accommodation for the two cleavage cracks on either side of the boundary. Therefore the area of accommodation fracture simply grows outward from the crack intersections with the boundary. The end product of this process is that the whole of the grain boundary is fractured, which is not physical.

Putting all the bits of the model together, Fig. 11 shows cleavage propagation through a model with 20 grains, after 300 cleavage iterations. Note that a significant fraction of grains exhibit multiple cracks on parallel planes. Since the model explicitly forbids more than one crack to

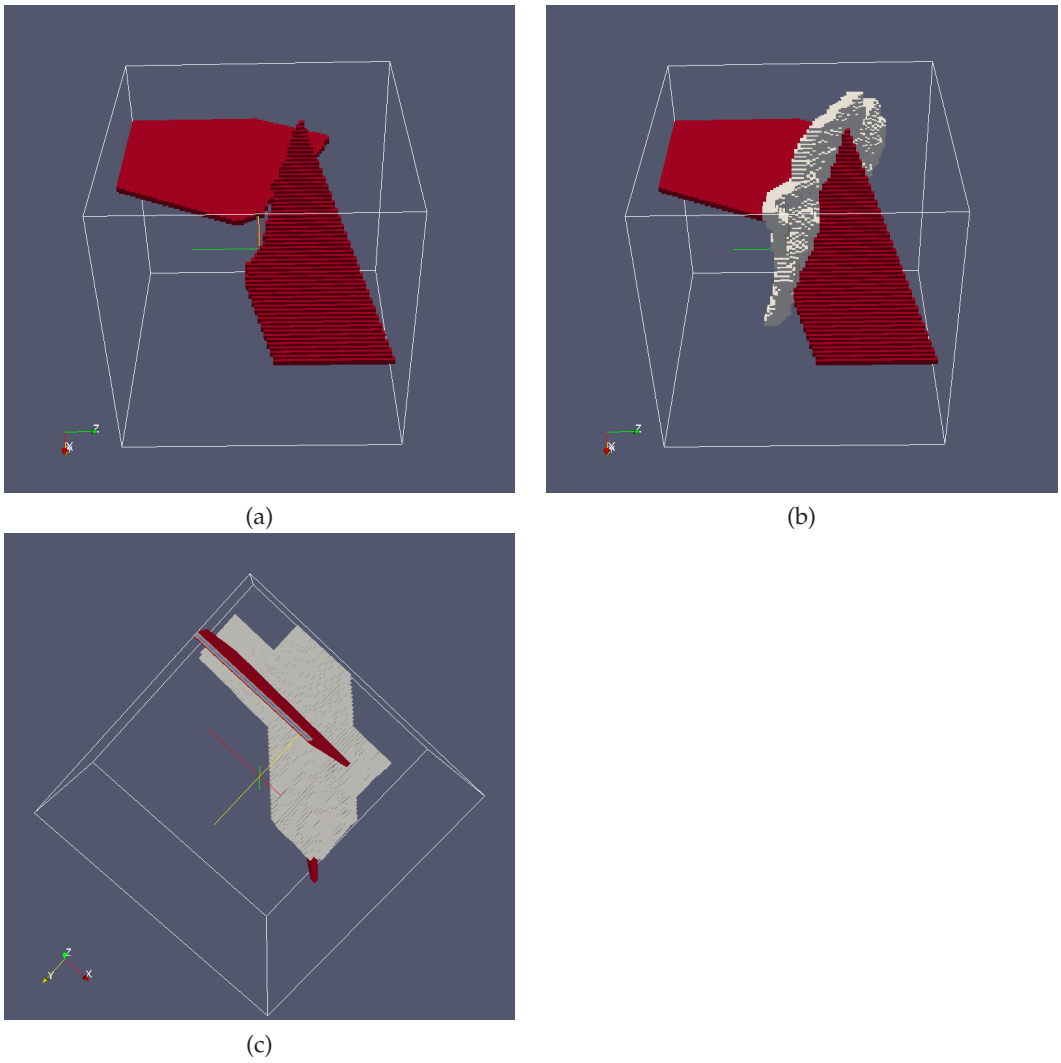

Figure 10. A model with two grains, showing (a) the two {110} cleavage cracks in two grains. Neither the grains nor the grain boundary are shown for clarity; (b) same view as in (a) but with the fractured part of the grain boundary also shown, and (c) a different view of the fractured grain boundary. Note that the fractured grain boundary area simply grows away from the intersection locations with each iteration. The end result of this process is that the whole of the grain boundary is fractured, which is not physically sound.

propagate across any grain boundary, this means that cracks propagates into these grains from different boundaries. For example, refer to Fig. 11(c). A grain in the front bottom corner of the model has 3 cleavage cracks. It is likely that one of these cracks propagated into this grain from the grain to its top left, and the other two cracks propagated from the two grains to its right. Note that this example did not include the feedback from the microstructure to the structural model, i.e. there is was no reduction of $\mathbf{t}^s$ in cracked grains. In practice, a cracked grain would receive a dramatically reduced $\mathbf{t}^s$, making further cracks on the same crystallographic planes very unlikely.

7. Combining with finite elements for a multi-scale model

A complete CAFE (cellular automata finite element) multi-scale model was constructed by linking the CA model with the ParaFEM finite element library [40,41]. Conventional localisation and

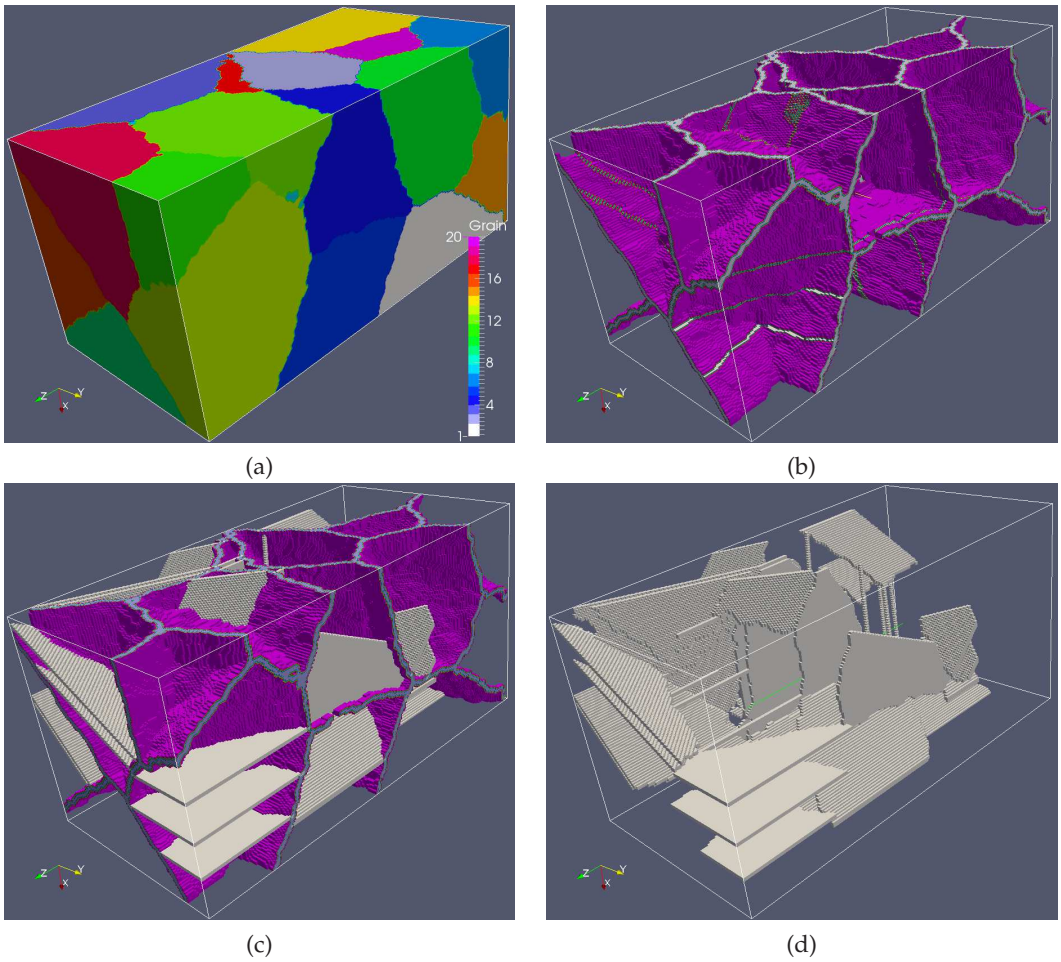

Figure 11. A cleavage propagation example with 20 grains, showing: (a) grains and grain boundaries on the surface of the model, (b) 3D view of grain boundaries in the interior of the model, (c) cleavage cracks superimposed on grain boundaries, and (d) only cleavage cracks, with all other structures removed for clarity.

homogenisation strategies [18,26,42] can then be used to exchange the information between the FE and the CA parts of the model. In this example the FE stress tensor was redistributed over the CA according to the proximity of the cells to crack flanks, to replicate the stress intensity dominated stress fields. Cells closest to the crack flanks receive much higher stress tensors than the FE value. Cells sufficiently removed from crack flanks receive lower stress tensors than the FE value. The mean value of the CA stress tensors is equal to the FE stress tensor. The homogenisation is done via scaling of the FE Young's modulus according to the size of the cleavage crack. A representative example is given below.

A $10 \times 10 \times 10\text{mm}^3$ cube of material is considered. The material model is linear elastic, with the Young's modulus of 200GPa. The boundary conditions are: $u_1(x_1 = 0) = 0$, $u_2(x_2 = 0) = 0$, $u_3(x_3 = 0) = 0$. Distributed loading is applied along x_3 on a small element of surface $x_3 = 10$, with the total applied force of 1kN. The mean grain diameter is taken as high as 1mm, primarily to ease the visualisation, because large grains result in large trans-granular cracks. The complete model thus implements 1,000 randomly oriented grains. A single micro-crack is introduced at $x_1 = x_2 = 0$, $x_3 = 5$mm. The results in Fig. 12 show the deformed finite element mesh and the crack patterns produced in three runs of the model.

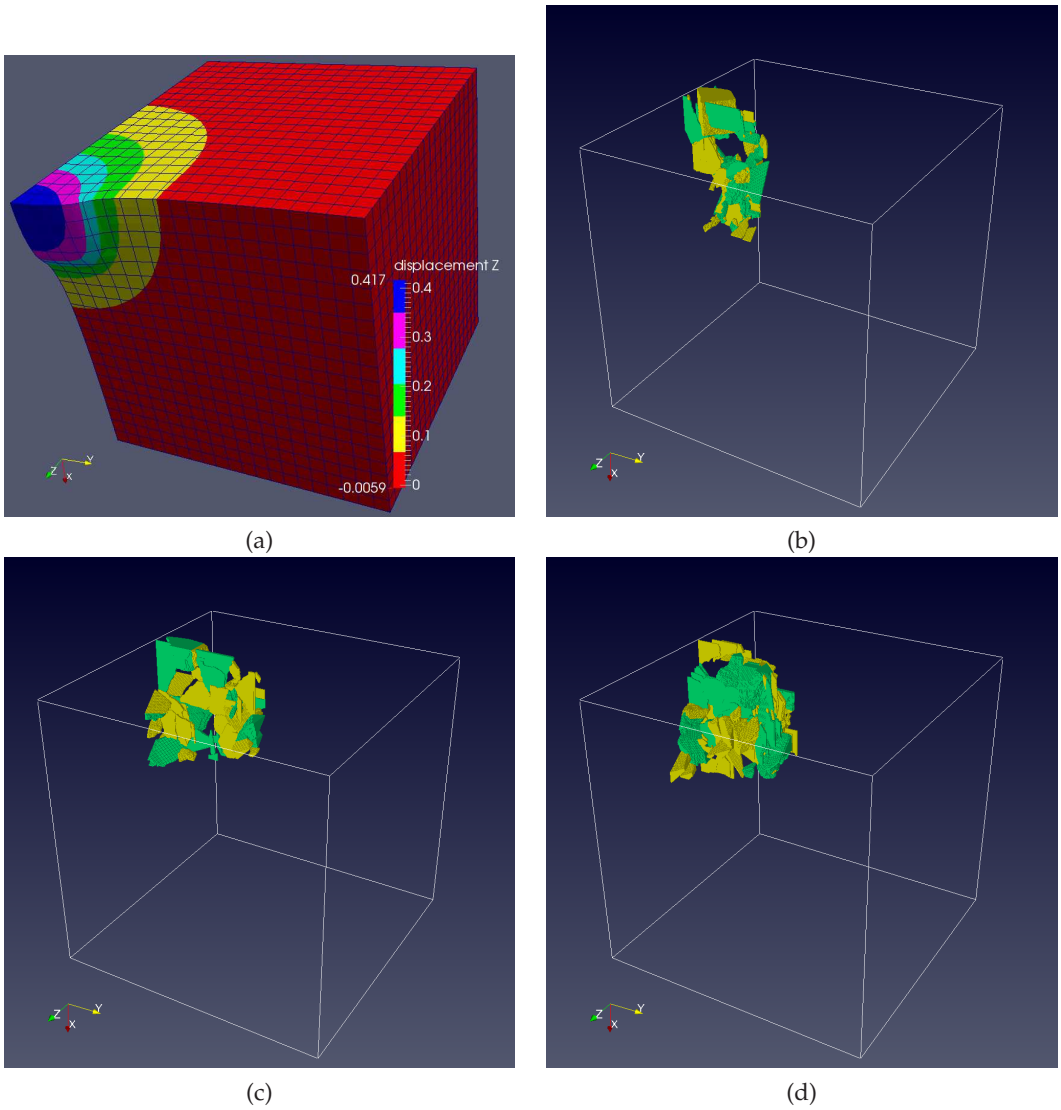

Figure 12. Three runs of a CAFE model in a steel-like material with large grains, showing: (a) the deformed finite element model with the distortion artificially magnified for clarity, (b), (c) and (d) clusters of cracks on 100 planes (light gray or yellow online) and on 110 planes (dark gray or green online) forming a large main crack that is macroscopically normal to the maximum principal stress direction in that region. Each particular crack scenario is unique. Analysis of a statistically significant number of runs of this CAFE model can lead to the prediction of scatter in cleavage crack propagation results, such as the fracture energy.

8. Concluding remarks and future work

The 3D cellular automata framework, designed and implemented as described, has been shown to be capable of simulating progressive quasi-cleavage propagation though a polycrystal. The model is based on the fracture stress criterion and is made mesh independent by including a length scale. The model takes into account random orientations of individual crystals. The immediate next step is to add orientation dependent grain boundary energies [43,44]. Energies of the cleavage cracks might at first be taken equal to free surface energies, γ_{hkl}. Then the total energies of fracture can be calculated simply by summing the number of cells of cleavage states, c_{hkl}, and of grain boundary fracture states, c_{gb}, multiplied by their energies. In this respect 1D and 3D crack artifacts present

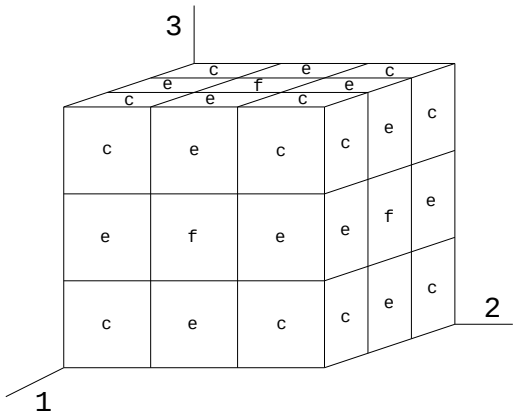

Figure 13. This $3 \times 3 \times 3$ cluster of 27 cubic cells represents the 26-cell nearest neighbourhood of the central cell. 6 neighbours share a face ("f"), 12 neighbours share an edge ("e") and 8 neighbours share a corner ("c"). A Cartesian CS is a natural choice for this model.

a major obstacle. 1D line crack artifacts will result in artificially low energy, and 3D solid body crack artifacts will dramatically increase the fracture energy. Hence, it is necessary to resolve the issue on non-physical 1D and 3D cracks if realistic fracture energy prediction is aimed for.

Data accessibility. All data is accessible from http://sourceforge.net/projects/cgpack/.

Disclaimer. AS contributed to all sections. LM contributed to the creation of the CAFE model, Sec. 7. Both authors gave final approval for publication.

Acknowledgements. This work used the ARCHER UK National Supercomputing Service (http://www.archer.ac.uk). This work also used HECToR, the UK's national high-performance computing service, which was provided by UoE HPCx Ltd at the University of Edinburgh, Cray Inc and NAG Ltd. HECToR was funded by the Office of Science and Technology through EPSRC's High End Computing Programme. This work also used the computational facilities of the Advanced Computing Research Centre, the University of Bristol (http://www.bris.ac.uk/acrc/) and the N8HPC Service, funded by the N8 consortium and EPSRC EP/K000225/1, coordinated by the Universities of Leeds and Manchester (http://n8hpc.org.uk).

Conflict of interests. We have no competing interests.

A. Resolving arbitrary plane within a 3D CA cell neighbourhood

In 3D CA a cell has 26 nearest neighbours: 6 share a common face, 12 share a common edge and 8 share a common corner (vertex), see Fig. 13. This 3D space partitioning scheme is popular in CA because it is particularly easy to visualise and implement in a computer program, simply by using a three-dimensional array.

A Cartesian CS, with arbitrary origin, is aligned with cell axes. In single or poly-crystal models a crystal is represented by a cluster of cells. A crystal can have arbitrary orientation with respect to the global (cellular) CS. In contrast the cell neighbourhood can be discretised only into 26 directions, one for each neighbouring cell. Thus a problem arises when crystallographic directions or planes have to be resolved within discrete cellular models.

A problem of particular importance is trans-granular cleavage, where material is separated along a crystallographic plane, e.g. {100} or {110} plane in bcc crystals. To simulate cleavage in a cellular model one must answer this question for every cell: which neighbouring cells are on the cleavage plane?

Let's illustrate the problem on a two-dimensional example, see Fig. 14. Let $\mathbf{n}$ be the unit vector normal to some cleavage plane, and $\mathbf{e}^i, i = 1 \dots 8$, is a unit vector connecting a cell with one of

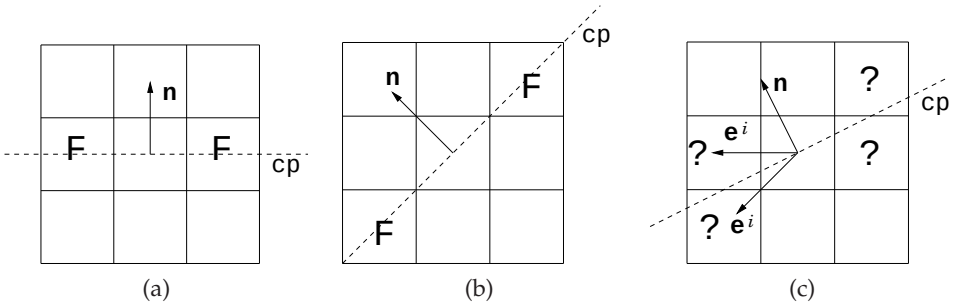

Figure 14. Two-dimensional illustration of the problem of deciding which neighbouring cells are on the cleavage plane (cp, defined by its normal, $\mathbf{n}$). When $\mathbf{n}$ is aligned with one of the cell direction vectors, $\mathbf{e}^i$, the answer is clear because the cleavage plane passes directly through the centres of two neighbouring cells ("F" for failed), as in cases (a) and (b). In general, no $\mathbf{e}^i$ vectors are normal to $\mathbf{n}$, and it is unclear which, if any, cells (marked "?") should be considered to lie on the cleavage plane. Possible answers are zero, two or four.

its 8 neighbours. If $\mathbf{n} \cdot \mathbf{e}^i = 0$, for any i then the question of which neighbouring cells are on the cleavage plane is trivial, see Fig. 14(a) and (b). In general case, the answer to this question is not clear. To help us answer it in general case, we pose this problem: find $\mathbf{n}$ that would maximise the minimum angle between the cleavage plane and each of $\mathbf{e}^i$. This problem is solved by finding $\max_{\mathbf{n}}(\min_{i=1\ldots8} |\mathbf{n} \cdot \mathbf{e}^i|)$, which we denote z. Looking at Fig. 14(c) this 'MaxMin' criterion corresponds to the cleavage plane at equal angles to two adjacent cell direction vectors. Therefore the angle is $\theta = \pi/8 = 22.5^\circ$, $\mathbf{n} = (\cos(\theta + m\frac{\pi}{4}), \sin(\theta + m\frac{\pi}{4}))$ for any integer m and $z \approx 0.38$.

One can then construct a cleavage criterion based on θ or z. One possible criterion can be that a neighbouring cell i is considered to lie on the cleavage plane if $|\mathbf{n} \cdot \mathbf{e}^i| \leq z$.

In three-dimensional case this analysis is more complex. If the centre of the central cell in Fig. 13 is given coordinates $(0, 0, 0)$, then the directions to centres of the neighbouring cells are given by the following 26 unit vectors, $\mathbf{e}^i$, $i = 1 \ldots 26$. There are six common face cells: $(\pm1, 0, 0)$, $(0, \pm1, 0)$, $(0, 0, \pm1)$; twelve common edge cells: $(\pm1/\sqrt{2}, \pm1/\sqrt{2}, 0)$, $(0, \pm1/\sqrt{2}, \pm1/\sqrt{2})$, $(\pm1/\sqrt{2}, 0, \pm1/\sqrt{2})$, and eight corner cells: $(\pm1/\sqrt{3}, \pm1/\sqrt{3}, \pm1/\sqrt{3})$. Consider an arbitrary unit vector $\mathbf{n}$. We formulate two geometric problems.

Problem 1: find $\max_{\mathbf{n}}(\min_{i=1\ldots26} |\mathbf{n} \cdot \mathbf{e}^i|)$ for all possible $\mathbf{n}$.

Problem 2: find $\min_{\mathbf{n}}(\max_{i=1\ldots26} |\mathbf{n} \cdot \mathbf{e}^i|)$ for all possible $\mathbf{n}$.

Although only problem 1 is related to the cleavage analysis, problem 2 is the opposite of problem 1, so we solve it as well.

(a) Problem 1

Fig. 15 shows that the model has 3 planes of symmetry. It is therefore sufficient to choose $\mathbf{n}$ only from one coordinate corner. For simplicity, we choose the corner with all coordinate axes positive. If $\mathbf{n} = (n_1, n_2, n_3)$ solves problem 1, then so do the eight vectors $(\pm n_1, \pm n_2, \pm n_3)$. Furthermore, because the problem is symmetrical with any permutation of the coordinate axes, a further six vectors are obtained from each $\mathbf{n}$ by permutation of its components. In total there are 48 vectors $\mathbf{n}$ which solve problem 1.

Refer to Fig. 15. The origin is at the central cell and the unit vectors show locations of the centres of some of the neighbouring cells. Due to three symmetry planes the space can be divided as left/right, top/bottom and front/back. In this terminology $\mathbf{n}$ is in the right top front corner. The problem is that of finding $\mathbf{n}$ that makes biggest angles (but $< \pi/2$) with three $\mathbf{e}^i$ vectors. The first vector can be chosen arbitrarily. We choose $\mathbf{e}^1 = (0, 0, 1)$. To maximise the angles between $\mathbf{n}$, the other two vectors must lie in other corners. In the right bottom front corner, vector making the biggest angle with $\mathbf{n}$ is either $(0, 1/\sqrt{2}, -1/\sqrt{2})$ or $(1/\sqrt{2}, -1/\sqrt{2}, 0)$. We choose the first of these: $\mathbf{e}^2 = (0, 1/\sqrt{2}, -1/\sqrt{2})$. This leaves the third vector from left bottom front corner,

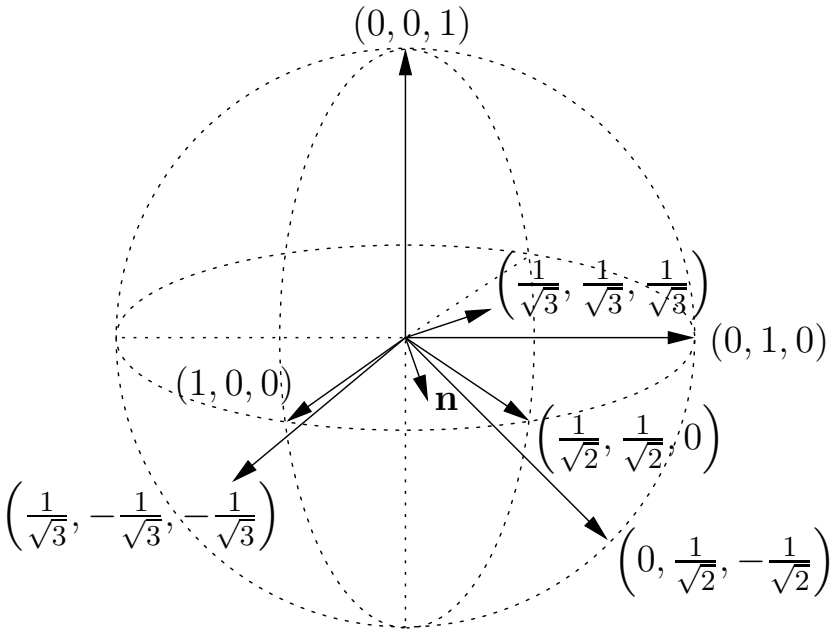

Figure 15. Schematic illustration of cell direction vectors, $\mathbf{e}^i, i = 1 \ldots 26$. The central cell is at the origin. Unit vectors connect the central cell with the centres of its neighbours. Only vectors used in the solution of the problems are shown.

$\mathbf{e}^3 = (1/\sqrt{3}, -1/\sqrt{3}, -1/\sqrt{3})$. All other vectors in the front corners are either reflections of the chosen vectors about the symmetry planes, or make smaller angles with $\mathbf{n}$, or angles $> \pi/2$ with $\mathbf{n}$. The problem is then reduced to solving the following equations.

$$\mathbf{n} \cdot \mathbf{e}^1 = \mathbf{n} \cdot \mathbf{e}^2; \qquad \mathbf{n} \cdot \mathbf{e}^2 = \mathbf{n} \cdot \mathbf{e}^3 \tag{A 1}$$

for n_1 and n_2; $n_3^2 = 1 - n_1^2 - n_2^2$. We omit the algebra and give the solution:

$$n_1 = \rho n_2; \qquad n_2 = \left(\frac{2\,(2+\sqrt{2})}{3+2\sqrt{2}} + \rho^2 \right)^{-1/2} \qquad \text{where} \qquad \rho = \frac{2+\sqrt{3}+\sqrt{2}}{1+\sqrt{2}} \tag{A 2}$$

This gives $\mathbf{n} \approx (0.8916, 0.4183, 0.1733)$ or any of its 47 equivalents constructed as discussed above. Solution to problem 1 is then

$$\max_{\mathbf{n}} \left(\min_{i=1\ldots26} |\mathbf{n} \cdot \mathbf{e}^i| \right) \approx 0.1733. \tag{A 3}$$

(b) Problem 2

Again refer to Fig. 15. We are now looking for $\mathbf{n}$ such that it makes the biggest possible angles (but $< \pi/2$) with closest vectors $\mathbf{e}$. We choose $\mathbf{e}^1 = (1, 0, 0)$. Its two closest vectors in the same corner are: $(1/\sqrt{2}, 1/\sqrt{2}, 0)$ or $(1/\sqrt{2}, 0, 1/\sqrt{2})$. We choose the first of these: $\mathbf{e}^2 = (1/\sqrt{2}, 1/\sqrt{2}, 0)$. The only choice for the third closest vector in the same corner is $\mathbf{e}^3 = (1/\sqrt{3}, 1/\sqrt{3}, 1/\sqrt{3})$. As in problem 1, we then solve Eqns. (A 1). The answer is:

$$n_1^2 = 9 - 2(\sqrt{6} + \sqrt{2}); \qquad n_2 = n_1(\sqrt{2} - 1) \tag{A 4}$$

This gives $\mathbf{n} \approx (0.8865, 0.3672, 0.2817)$ or any of its 47 equivalents constructed as discussed above. Solution to problem 2 is then:

$$\min_{\mathbf{n}}(\max_{i=1\ldots26}|\mathbf{n}\cdot\mathbf{e}^i|)\approx 0.8865. \tag{A 5}$$

References

1. G. Y. Vichniac.
   Simulating physics with cellular automata.
   Physica D, 10(1-2):96–116, 1984.
2. B. Chopard and M. Droz.
   Cellular Automata Modeling of physical systems.
   Cambridge, 1998.
3. R. LeSar.
   Computational Materials Science.
   Cambridge, 2013.
4. A. Shterenlikht and I. C. Howard.
   The CAFE model of fracture – application to a TMCR steel.
   Fatigue and Fracture of Engineering Materials and Structures, 29:770–787, 2006.
5. S. Das, A. Shterenlikht, I. C. Howard, and E. J. Palmiere.
   A general method for coupling microstructural response with structural performance.
   Proceedings of the Royal Society A, 462(2071):2085–2096, 2006.
6. J. Phillips, A. Shterenlikht, and M. J. Pavier.
   Cellular automata modelling of nano-crystalline instability.
   In *Proceedings of the 20th UK Conference of the Association for Computational Mechanics in Engineering, 27-28 March 2012, The University of Manchester, UK*, 2012.
   http://eis.bris.ac.uk/~mexas/pub/2012_ACME.pdf.
7. G. Guillemot, Ch.-A. Gandin, and M. Bellet.
   Interaction between single grain solidification and macro segregation: Application of a cellular automaton - Finite element model.
   Journal of Crystal Growth, 303:58–68, 2007.
8. T. Carozzani, H. Digonnet, and Ch-A. Gandin.
   3D CAFE modeling of grain structures: application to primary dendritic and secondary eutectic solidification.
   Modelling and Simulation in Materials Science and Engineering, 20:015010, 2012.
9. R. S. Saluja, R. G. Narayanan, and S. Das.
   Cellular automata finite element (CAFE) model to predict the forming of friction stir welded blanks.
   Comp. Mat. Sci., 58:87–100, 2012.
10. D. Raabe.
    Introduction of a scalable three-dimensional cellular automaton with a probabilistic switching rule for the discrete mesoscale simulation of recrystallization phenomena.
    Philosophical Magazine A, 79:2339–2358, 1999.
11. D. Raabe and R. C. Becker.
    Coupling of a crystal plasticity finite-element model with a probabilistic cellular automaton for simulating primary static recrystallization in aluminium.
    Modelling and Simulation in Materials Science and Engineering, 8:445–462, 2000.
12. D. Raabe.
    Cellular automata in materials science with particular reference to recrystallization simulation.
    Annual Review of Materials Research, 32:53–76, 2002.
13. C. Zheng and D. Raabe.
    Interaction between recrystallization and phase transformation during intercritical annealing in a cold-rolled dual-phase steel: A cellular automaton model.
    Acta Materialia, 61:5504–5517, 2013.
14. C. Zheng, D. Raabe, and D. Li.
    Prediction of post-dynamic austenite-to-ferrite transformation and reverse transformation in a low-carbon steel by cellular automaton modeling.
    Acta Materialia, 60:4768–4779, 2012.

15. G. E. Smith, A. G. Crocker, P. E. J. Flewitt, and S. Mahalingam.
Creating three-dimensional models to investigate brittle fracture in polycrystalline metals.
CMC-COMPUTERS MATERIALS & CONTINUA, 31(1):17–36, 2012.
16. G. M. Hughes, G. Smith, A. G. Crocker, and P. E. J. Flewitt.
An examination of the linkage of cleavage cracks at grain boundaries.
Materials Science and Technology, 21(11):1268–74, 2005.
17. A. G. Crocker, P. E. J. Flewitt, and G. E. Smith.
Computational modelling of fracture in polycrystalline materials.
International Materials Reviews, 50(2):99–124, 2005.
18. J.-P. Mathieu, S. Berveiller, K. Inal, and O. Diard.
Microscale modelling of cleavage fracture at low temperatures: influence of heterogeneities at the granular scale.
Fatigue Fract Engng Mater Struct, 29:725–737, 2006.
19. S. Falco, P. Siegkas, E. Barbieri, and N. Petrinic.
A new method for the generation of arbitrary shaped 3d random polycrystalline domains.
Comput Mech, 54:1447–1460, 2014.
20. S. R. Phillpot, J. Wang, D. Wolf, and H. Gleiter.
Computer simulation of the structure and dynamical properties of grain boundaries in a nanocrystalline model material.
Mat Sci Engineering A, 204:76–82, 1995.
21. Da Chen.
Structural modeling of nanocrystalline materials.
Computational Materials Science, 3:327–333, 1995.
22. J. J. Gilman.
Cleavage, ductility and tenacity in crystals.
In Averbach et al. [45], pages 193–224.
23. A. H. Cottrell.
Theoretical aspects of fracture.
In Averbach et al. [45], pages 20–53.
24. R. Khare, S. L. Mielke, J. T. Paci, S. Zhang, R. Ballarini, G. C. Schatz, and T. Belytschko.
Coupled quantum mechanical/molecular mechanical modeling of the fracture of defective carbon nanotubes and graphene sheets.
Phys. Rev. B, 75:75412, 2007.
25. O. A. Shenderova, D. W. Brenner, A. Omeltchenko, X. Su, and L. H. Yang.
Atomistic modeling of fracture of polycrystalline diamond.
Phys. Rev. B, 61:3877–3888, 2000.
26. F. Roters, P. Eisenlohr, L. Hantcherli, D. D. Tjahjanto, T. R. Bieler, and D. Raabe.
Overview of constitutive laws, kinematics, homogenization and multiscale methods in crystal plasticity finite-element modeling: Theory, experiments, applications.
Acta Materialia, 58:1152–1211, 2010.
27. W. Gerberich and W. Yang, editors.
Comprehensive Structural Integrity. Volume 8: Interfacial and Nanoscale Failure.
Elsevier, 2003.
28. H. Liebowitz, editor.
Fracture. Volume 1: Microscopic and Macroscopic Fundamentals.
Academic Press, 1968.
29. J. R. Low.
A review of the microstructural aspects of cleavage fracture.
In Averbach et al. [45], pages 68–90.
30. ISO/IEC 1539-1:2010.
Fortran – Part 1: Base language, International Standard.
2010.
31. A. Shterenlikht.
Fortran coarray library for 3D cellular automata microstructure simulation.
In M. Weiland, A. Jackson, and N. Johnson, editors, *Proc. 7th PGAS Conf. Edinburgh, Scotland, UK*, pages 16–24, 2014.
http://www.pgas2013.org.uk/sites/default/files/pgas2013proceedings.pdf.
32. T. Lin, A. G. Evans, and R. O. Ritchie.

Stochastic modeling of the independent roles of particle size and grain size in transgranular cleavage fracture.
Met. Mat. Trans. A, 18:641–51, 1987.

33. J. K. Mackenzie.
Second paper on statistics associated with the random disorientation of cubes.
Biometrika, 45(1/2):229–40, 1958.
34. D. Romero, L. Martinez, and L. Fionova.
Computer simulation of grain boundary spatial distribution in a three-dimensional polycrystal with cubic structure.
Acta Materialia, 44(1):391–402, 1996.
35. H. Khanbareh and S. Wu, X. M. van der Zwaag.
Analysis of the fractal dimension of grain boundaries of aa7050 aluminum alloys and its relationship to fracture toughness.
Journal of Material Science, 47(17):6246–53, 2012.
36. O. A. Hilders, M. Ramos, N. D. Peña, and L. Sàenz.
Fractal geometry of fracture surfaces of a duplex stainless steel.
Journal of Material Science, 41(17):5739–42, 2006.
37. Y. Su and W. S. Lei.
Relationship between fracture toughness and fractal dimension of fracture surface of steel.
Int. J. Fract., 106(3):L41–L46, 2000.
38. J. C. Hsiung and Y. T. Chou.
Fractal characterization of the fracture surface of a high-strength low-alloy steel.
J. Mater. Sci., 33(11):2949–53, 1998.
39. B. B. Mandelbrot.
The fractal geometry of nature.
W. H. Freeman and Company, 1983.
40. ParaFEM - A General Parallel Finite Element Message Passing Library, Research Computing Services, The University of Manchester, UK, 2015.
http://www.parafem.org.uk/ (HTML).
41. I. M. Smith, D. V. Griffiths, and Margetts. L.
Programming the Finite Element Method.
Wiley-Blackwell, 5 edition, 2014.
42. C. C. Tasan, J. P. M. Hoefnagels, M. Diehl, D. Yan, F. Roters, and D Raabe.
Strain localization and damage in dual phase steels investigated by coupling in-situ deformation experiments and crystal plasticity simulations.
Int. J. Plast., 63:198–210, 2014.
43. J. D. Rittner and D. N. Seidman.
$\langle 110 \rangle$ symmetric tilt grain-boundary structures in fcc metals with low stacking-fault energies.
Physical Review B, 54(10):6999–7015, 1996.
44. G. Hasson, J.-Y. Boos, I. Herbeuval, M. Biscondi, and C. Goux.
Theoretical and experimental determinations of grain boundary structures and energies: correlation with various experimental results.
Surface Science, 31:115–137, 1972.
45. B. L. Averbach, D. K. Felbeck, G. T. Hahn, and D. A. Thomas, editors.
Fracture. Proceedings of an International Conference on the Atomic Mechanisms of Fracture held in Swampscott, Massachusetts, April 12-16, 1959. The Technology Press of Massachusetts Institute of Technology and John Wiley & Sons, New York, 1959.